Research Square

Preprints are preliminary reports that have not undergone peer review.
They should not be considered conclusive, used to inform clinical practice,
or referenced by the media as validated information.

Composite load-bearing behavior and weakening-induced fracturing mechanisms of close distance thick-hard roofs in thick coal seam

Xiaowu Zhang

Zhxw667@163.com

Lyuliang University

Yue Cao

China University of Mining and Technology

Lei Shi

Lyuliang University

Lianhai Tai

Anhui University of Science and Technology

Zhibing Liu

Shaanxi Binchang Dafosi Mining Co., Ltd, Shaanxi Shanmei Group

Xiaojun Li

Shanxi Pingshang Coal Co., Ltd

Research Article

Keywords: Close distance thick-hard roofs, Combined load-bearing, Energy release, Fracture-induced weakening, Mine pressure bump

Posted Date: November 25th, 2026

DOI: https://doi.org/10.21203/rs.3.rs-11682921/v1

License: This work is licensed under a Creative Commons Attribution 4.0 International License.
Read Full License

Additional Declarations: No competing interests reported.

Composite load-bearing behavior and weakening-induced fracturing mechanisms of close distance thick-hard roofs in thick coal seam

Xiaowu Zhang[a, *], Yue Cao[b], Lei Shi[a], Lianhai Tai[c], Zhibing Liu[d], Xiaojun Li[e]

[a] Department of Resource and Mechanical Engineering, Lyuliang University, Lvliang, Shanxi, 033001 China ;

[b] School of Mines, China University of Mining and Technology, Xuzhou, Jiangsu, 221116, China;

[c] School of Mining Engineering, Anhui University of Science and Technology, Huainan, Anhui, 232001, China

[d] Shaanxi Binchang Dafosi Mining Co., Ltd., Shaanxi Shanmei Group, Binzhou, Shaanxi, 713500, China

[e] Shanxi Pingshang Coal Co., Ltd., Jinneng Holding Group, Jincheng, Shanxi, 048000, China

***Corresponding author:**

E-mail address: Zhxw667@163.com(X. Zhang)

Funding information:

This work was supported by the Key Projects of Joint Fund of the National Natural Science Foundation of China(Grant Number: U21A20107); the Young Scientists Fund of the National Natural Science Foundation of China (Grant Number: 52404147); the Fundamental Research Funds for the Central Universities(Grant Number: 2025ZDPY03) and the Special-funded Project for High-level Scientific and Technological Talents of Lvliang City (Grant No. 2024RC26).

Abstract: During coal extraction beneath close distance thick-hard roofs(CDTHR), stopes and roadways experience severe stress environments, making them prone to intense strata behavior and dynamic hazards. This study investigated the combined load-bearing characteristics of stope overlain by CDTHR, derived the mechanical criteria governing the ultimate fracturing of CDTHR, and revealed the fracture-induced weakening mechanisms of CDTHR. A staged, directional long-borehole hydraulic fracturing technology was proposed for the stope overlain by CDTHR. The results indicate CDTHR act as core load-bearing and energy-storing elements within the overburden. The ultimate load-bearing capacity of CDTHR decreases progressively with an increase in the overhanging span and a decrease in the maximum principal stress. When CDTHR located at greater distances from the coal seam fracture, the degradation of the combined load-bearing capacity becomes more pronounced. Implementation of the staged directional long-borehole hydraulic fracturing technology effectively reduces the periodic weighting interval and spatial extent of the working face, disrupts the continuity of high-stress concentration zones, mitigates the violent release of strain energy, and substantially alleviates severe ground-pressure hazards.

Key words: Close distance thick-hard roofs; Combined load-bearing; Energy release; Fracture-induced weakening; Mine pressure bump

0 Introduction

Coal serves as the cornerstone energy source ensuring China's energy security and sustaining the stable operation of its national economy (He et al,2021;Yu et al,2025; Wu et al, 2026). Despite the rapid expansion of the renewable energy sector, coal will remain the dominant component of China's energy mix for the foreseeable future, governed by national resource endowments as well as technical and economic constraints(Zhang et al, 2022; Bai et al, 2017; Wu et al, 2020). Driven by long-term coal-forming geological processes, major coal-producing regions in China—such as Shanxi, Shaanxi, and Inner Mongolia—are predominantly characterized by coal seams overlain by thick-hard roofs(THR)(Xue et al, 2025; Tian et al, 2024). These THR above

the stope exhibit high structural integrity, substantial flexural rigidity, and high load-bearing capacity(Jing et al, 2024; Li et al, 2014; He et al, 2016). Consequently, they fail to cave in a timely manner as the longwall face advances, frequently resulting in extensive overhanging roof structures above the goaf(Han et al, 2015; Zhao et al, 2022). Under the combined action of self-weight and overburden loading, the suspended THR undergo continuous bending deformation, accumulating massive elastic strain energy(Wang et al, 2020; Lin et al, 2016;Xu et al, 2016). When the cantilever span reaches the critical threshold, these THR undergo sudden, large-scale (or monolithic) fracturing and caving(Shen et al, 2016; Lu et al, 2015; Zhang et al, 2010). The instantaneous release of the stored strain energy induces severe dynamic hazards, such as support crushing, leg penetration into the floor, intense ground pressure manifestations, and structural failure of surrounding roadways(Yang et al, 2023; Xie et al, 2022). Such hazards pose serious threats to the safety of underground personnel and equipment, significantly hindering the safe and efficient extraction of coal resources(Bai et al, 2024; Wu et al, 2021; Guo et al, 2019).

Extensive research has been conducted on the fracture behaviors of THR in stopes and their corresponding hazard mitigation technologies. Taking the 24110 working face of Nanyangpo Coal Mine as a case study, Liu et al proposed a combined strategy integrating shallow-hole dense blasting with deep-hole directional pressure relief based on full-roadway roof pre-splitting. Field implementation demonstrated that the initial caving interval of the working face was reduced by 20 m compared to untreated conditions, accompanied by a significant reduction in peak stress concentration along the coal rib and stope roof. Shan et al developed a liquid-nitrogen fracturing method for THR and applied it to the 1302 working face of Zhujiamao Coal Mine. Field verification confirmed that this technique generates multi-scale fracture networks within the THR, thereby reducing its stiffness and structural strength to promote stable caving over shorter spans. Focusing on a 16 m thick-hard sandstone roof at the 11129 working face of Zhangji Coal Mine, Dang et al investigated strata deflection, roof support interactions, and the mechanics of artificial roof detachment following pre-split blasting using combined physical modeling and numerical simulations; their results revealed that pre-split blasting substantially lowered peak roof stresses and effectively dissipated coal rib stress. Fu et al introduced a combined blasting technique integrating directional and non-directional charges for THR at the 122108 working face of Caojiatan Coal Mine. This approach effectively cuts the roof strata to form a controlled cantilever beam structure, reducing overall stope stress and disrupting stress transfer pathways. Using numerical simulations, Zhang et al investigated the effects of advancing mining stages on the stress, displacement, and energy fields of thick, competent roofs in deep, ultra-thick coal seams; they observed that roof stresses increased progressively with face advance, forming localized high-energy zones where shear fracturing dominated the failure pattern and expanded in scale as mining advanced. Additionally, Zhang et al modeled the blast-induced fracturing process of high-position THR at the 6306 working face of Dongtan Coal Mine. Their findings

showed that the failure of high-position THR releases substantial strain energy into the goaf, whereas controlled pre-split blasting promotes localized fracturing in the overburden, thereby significantly mitigating main roof weighting intensity across the working face.

As an effective method for inducing artificial fracture networks, hydraulic fracturing has been widely applied to weaken and break THR in underground coal mining. Fan et al systematically investigated the mechanisms of rockburst prevention via hydraulic fracturing using theoretical analysis and numerical simulations, demonstrating a marked reduction in stress concentration within the coal seam at the 6305 working face of Jisan Coal Mine. Guo et al analyzed the spatiotemporal evolution of roof subsidence in ultra-thick coal seams overlain by THR under varying mining-to-caving ratios at the 8401 working face of Tongfa Dongzhouyao Coal Mine; their findings revealed that hydraulic fracturing effectively degrades thick-hard sandstone roofs and creates pre-damaged fracture zones, thereby enabling predictable and controllable roof caving. Investigating the MC Coal Mine, Zhao et al characterized overburden movement, fracture propagation, structural failure, and stress evolution in a stope overlain by a near-field competent roof, observing a significant drop in microseismic event frequency post-fracturing. For the 2803 goaf-adjacent working face of Hetaoyu Coal Mine, Zhang et al conducted a comparative analysis of the stress field, elastic strain energy field, and damage distribution ahead of the longwall face under both non-fractured and hydraulically fractured conditions. Microseismic monitoring confirmed that hydraulic fracturing forms a patchy, locally interconnected high-damage zone within the THR, effectively reducing its overall structural strength. Yao et al evaluated deep thick-hard roof pressure-relief technology using hydraulic fracturing at the 1012006 working face of Yuanzigou Coal Mine, showing substantial reductions in both the frequency and total energy release of microseismic events, along with a notable decrease in deep-seated roadway stress. Addressing multi-seam mining conditions, Wu et al analyzed overburden movement influenced by residual coal pillars and thick-hard roofs, proposing a staged hydraulic fracturing technique utilizing horizontal directional long boreholes; field applications confirmed that this approach effectively mitigates vertical stress concentrations on the coal face and preserves rib stability. Furthermore, Zou et al examined overburden fracture characteristics and microseismicity distributions before and after hydraulic fracturing tests at Dongtan Coal Mine, demonstrating a significant reduction in roof-induced mine seismicity. Zhuang et al implemented multi-stage hydraulic fracturing using horizontal directional wells in stopes overlain by THR, establishing overburden damage parameters to quantify roof-fracturing efficacy. Finally, Xia et al utilized physical similarity modeling to simulate the fracturing and caving processes of THR during longwall extraction, demonstrating that hydraulic fracturing suppresses the kinetic energy released during roof failure while reducing the overall load-bearing capacity of the THR.

Most existing studies have predominantly focused on the load-bearing behavior and disaster-inducing mechanisms of single-layer THR. However, when coal seams are

overlain by multi-layered, close distance thick-hard roofs(CDTHR), complex stress transfer and synergistic load-bearing interactions occur across different stratum horizons. Notably, following the fracture of lower key strata, overburden loads redistribute upward to the upper key strata. Consequently, applying analytical models developed for single-layer THR to multi-layered conditions fails to capture these load-transfer dynamics, leading to an underestimation of energy accumulation in the upper strata and leaving the stope vulnerable to severe dynamic ground-pressure hazards. To address this challenge, taking the CDTHR at the 31106 working face of Dafosi Coal Mine as a case study, This study investigated the combined load-bearing characteristics of stope overlain by CDTHR, derived the mechanical criteria governing the ultimate fracturing of CDTHR, and revealed the fracture-induced weakening mechanisms of CDTHR. A staged, directional long-borehole hydraulic fracturing technology was proposed for the stope overlain by CDTHR. This study provides theoretical guidance and engineering insights for mitigating roof hazards under similar geological conditions, offering significant practical value for ensuring safe and efficient underground coal mining.

1 Engineering Overview

The Dafosi Coal Mine is situated at the southern boundary of the Binchang Mining Area in Shaanxi Province, across the junction of Bin County and Changwu County. The coalfield spans approximately 15 km from east to west and 5.8 km from north to south, covering a total area of about 86.3 km². The mine field contains two minable coal seams, designated as No. 2 coal seam and No. 3 coal seam, with No. 3 coal seam serving as the primary mining seam, which exhibits a stable occurrence with a overall gentle inclination ranging from 5° to 10° (average 7°), making it a typical near-horizontal coal seam. The mine adopts a zonal layout divided into South and North wings. 31106 working face investigated in this study is located in the 31 Mining District within the South Wing.

The surface elevation above the 31106 working face ranges from 1495 m to 1504 m, while the underground extraction elevation varies from 1275 m to 1366 m, giving an average burial depth of 174.62 m. The working face has a designed face length of 178 m and utilizes a retreat longwall mining method from west to east, with a continuous extraction length of 2750 m. The working face is situated east of the main centralized rise entry of the mining area, with its open-off cut adjacent to the mine field boundary. The 31106 working face is located on the west side of the district centralized up-hill, with its initial cut adjacent to the western wing boundary of the 31 Mining District. The northern side is bounded by the succeeding 31108 working face, and the southern side is bordered by the mined-out adjacent 31104 working face. The surrounding mining layout is straightforward with clear geological conditions.. The geographical location and surrounding mining environment of the engineering site are illustrated in Fig. 1.

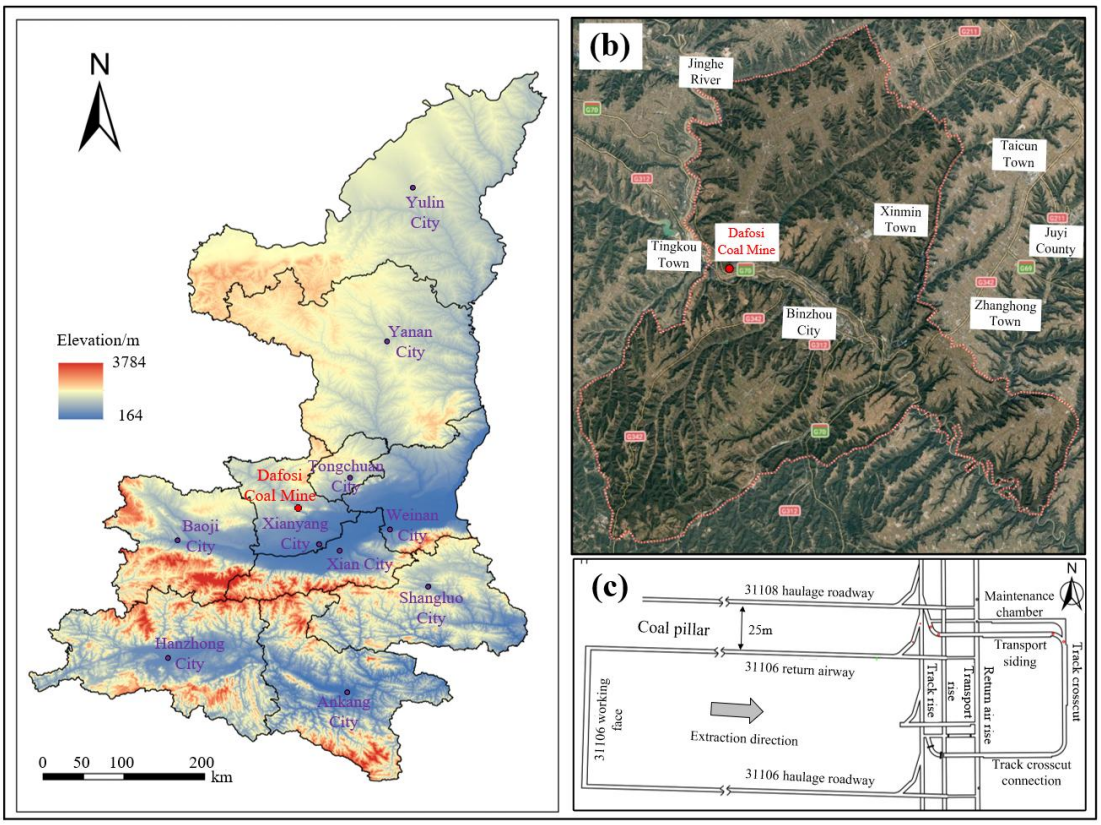

Fig. 1 Geographical location and surrounding conditions of stope: (a) geographical location, (b) administrative region, (c) surrounding conditions of stope

The primary mining seam of the 31106 working face, namely the No. 3 coal seam, is hosted within the Jurassic Datong Formation. Influenced by long-term tectonic movements and coal-forming processes, certain strata exhibit prominent characteristics of being thick, hard, and structurally competent. Drilling data indicate that multiple thick-hard sandstone roofs overlie the roof of the No. 3 coal seam. Specifically, a fine-grained sandstone layer with a thickness of 11.79 m is located 6.51 m above the coal seam roof, a coarse-grained sandstone layer with a thickness of 11.53 m is situated at a distance of 31.05 m, and a medium-grained sandstone layer with a thickness of 12.62 m occurs at 48.67 m. These three thick sandstone formations constitute the CDTHR of the overburden above the No. 3 coal seam longwall face, as illustrated in Fig. 2. During longwall extraction, these close distance thick-hard roofs(CDTHR) are prone to large breakage intervals and extensive overhanging roof areas, leading to the massive accumulation of elastic strain energy and readily triggering severe mining-induced strata behaviors. During the mining of the adjacent working face, the extensive influence range and high concentration of advanced abutment pressure frequently induced dynamic hazards such as support resistance overload, intense roof weighting, support leg penetration into the floor, and support crushing. These hazards severely disrupted normal mining operations and constrained safe, efficient coal production.

To effectively mitigate the severe ground-pressure hazards induced by the CDTHR, a fracture-induced weakening technology is adopted during the extraction of the 31106

working face. This technique artificially weakens the CDTHR to reduce their structural integrity, shorten the overhanging span, and degrade their load-bearing strength and energy-storage capacity. Consequently, it achieves the active release and transfer of roof stress, alleviates intense strata behaviors, eliminates safety hazards such as support crushing and floor penetration, improves stope surrounding rock control, and ensures the safe, stable, and efficient extraction of the working face.。

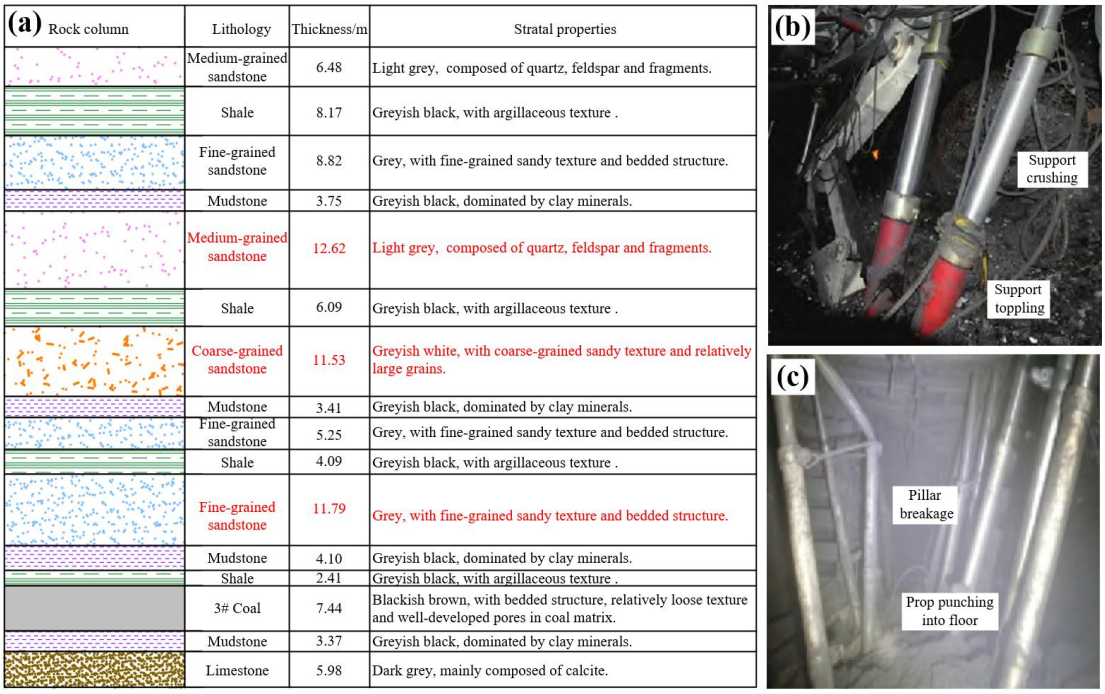

(a) Rock column	Lithology	Thickness/m	Stratal properties
	Medium-grained sandstone	6.48	Light grey, composed of quartz, feldspar and fragments.
	Shale	8.17	Greyish black, with argillaceous texture .
	Fine-grained sandstone	8.82	Grey, with fine-grained sandy texture and bedded structure.
	Mudstone	3.75	Greyish black, dominated by clay minerals.
	Medium-grained sandstone	12.62	Light grey, composed of quartz, feldspar and fragments.
	Shale	6.09	Greyish black, with argillaceous texture .
	Coarse-grained sandstone	11.53	Greyish white, with coarse-grained sandy texture and relatively large grains.
	Mudstone	3.41	Greyish black, dominated by clay minerals.
	Fine-grained sandstone	5.25	Grey, with fine-grained sandy texture and bedded structure.
	Shale	4.09	Greyish black, with argillaceous texture .
	Fine-grained sandstone	11.79	Grey, with fine-grained sandy texture and bedded structure.
	Mudstone	4.10	Greyish black, dominated by clay minerals.
	Shale	2.41	Greyish black, with argillaceous texture .
	3# Coal	7.44	Blackish brown, with bedded structure, relatively loose texture and well-developed pores in coal matrix.
	Mudstone	3.37	Greyish black, dominated by clay minerals.
	Limestone	5.98	Dark grey, mainly composed of calcite.

Fig. 2 Occurrence characteristics of CDTHR and manifestations of severe ground pressure in stope: (a) occurrence characteristics of CDTHR, (b) severe ground pressure manifestations in stope, (c) severe ground pressure manifestations in troadways.

2 Theoretical analysis of combined load-bearing for close distance thick-hard roofs

2.1 Theoretical model

Following coal extraction, the goaf is progressively formed, and the surrounding rock, originally in a state of equilibrium, begins to experience disturbance. As the working face advances, the roof strata above the goaf are continuously exposed, and their overhanging span increases steadily. The supporting effect of the coal seam on the roof strata progressively weakens, leading to a continuous increase in bending moments and tensile stress levels within the roof. When the internal stress reaches the ultimate load-bearing strength of the rock strata, the thick-hard roofs(THR) structure undergoes combined tensile-shear failure, causing the roof beam to lose its continuous load-bearing capacity and the rock blocks to cave. After the THR fractures, a portion of the caved rock blocks accumulates inside the goaf, providing support through the bulking and compaction effects of the goaf gangue. The remaining load is transferred upward to the working face, where it is jointly borne by the immediate roof and hydraulic supports, resulting in a significant increase in the working resistance of the supports

and triggering stope strata behavior. The overhanging span corresponding to THR fracture and instability is defined as the periodic weighting interval of the stope roof. Throughout the entire extraction cycle of the working face, the stope roof structure undergoes a repeating evolutionary loop of "load accumulation - fracture and caving - subsequent load accumulation," leading to persistent periodic weighting until the completion of mining. The mechanical model of the roof load-bearing structure for closely spaced key strata at this stage is illustrated in Fig. 3(a).

Upon the completion of longwall extraction, the un-fractured THR on the coal rib side of the working face, constrained by the surrounding coal and rock masses on both sides, can be mechanically abstracted as a cantilever beam structure with one end fixed and the other end free. The adjacent strata provide fixed constraints to the roof, bearing the bending moments and shear forces transmitted by the rock beam, while the goaf side lacks effective support, leaving the THR freely overhanging. This multi-layer composite cantilever beam system does not function as isolated single-layer rock beams; instead, loads are transferred among the high-position, middle-position, and low-position close distance thick-hard roofs(CDTHR) via intermediate interlayers. Concurrently, the deformation and loading of the low-position CDTHR are transmitted upward, influencing the stress states of the middle- position and high-position CDTHR. Multiple CDTHR jointly bear the overburden load, thereby constituting a composite roof load-bearing system. The mechanical model of the roof load-bearing system for CDTHR is illustrated in Fig. 3(b).

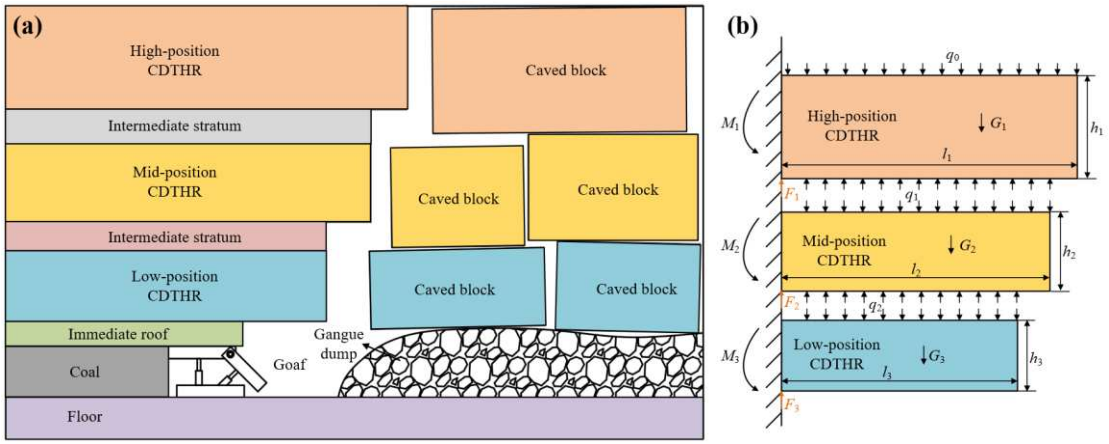

Fig. 3 Theoretical combined load-bearing models of CDTHR: (a) structural model, (b) mechanical model.

Note: q_0 is the uniformly distributed load applied by the upper overburden to the overall stope roof of the CDTHR, kN/m; q_1 and q_2 are the interaction loads between the contact interfaces of the high- position, middle- position, and low-position CDTHR in the stope, F_1、F_2 and F_3 are the supporting forces exerted by the adjacent rock mass on the high- position, middle- position, and low-position CDTHR, respectively, kN; G_1、G_2 and G_3 are the self-weights of the high- position, middle- position, and low-position CDTHR, respectively, kN; l_1、l_2 and l_3 are the overhanging roof lengths of the high-position, middle- position, and low-position CDTHR, respectively, m； h_1、h_2 and h_3

are the thicknesses of the high- position, middle- position, and low-position CDTHR, respectively, m； M_1、M_2 and M_3 are the bending moments exerted by the adjacent rock mass on the high- position, middle- position, and low-position CDTHR, respectively, kN/m.

2.2 Solution of model

As illustrated in Fig. 3, with the advance of coal extraction, the CDTHR in the stope gradually bear the load. By isolating the high-position key strata for mechanical analysis, its ultimate load-bearing state must satisfy the equilibrium conditions of forces and moments, as expressed in Eq. (1):

$$\begin{cases} q_0 l_1 + G_1 - F_1 - q_1 l_2 = 0 \\ \dfrac{q_0 l_1^{\,2}}{2} + \dfrac{G_1 l_1}{2} - \dfrac{q_1 l_2^{\,2}}{2} - M_1 = 0 \end{cases} \tag{1}$$

Similarly, by isolating the middle- position and low-position CDTHR for separate mechanical analysis, their respective limit equilibrium conditions can be expressed as Eqs. (2) and (3).

$$\begin{cases} q_1 l_2 + G_2 - F_2 - q_2 l_3 = 0 \\ \dfrac{q_1 l_2^{\,2}}{2} + \dfrac{G_2 l_2}{2} - \dfrac{q_2 l_3^{\,2}}{2} - M_2 = 0 \end{cases} \tag{2}$$

$$\begin{cases} q_2 l_3 + G_3 - F_3 = 0 \\ \dfrac{q_2 l_3^{\,2}}{2} + \dfrac{G_3 l_3}{2} - M_3 = 0 \end{cases} \tag{3}$$

Based on the principle of superposition beams, assuming that continuous contact is maintained across the contact interfaces among the high- position, middle- position, and low-position CDTHR in the stope during the load-bearing process, the bending moments among the closely spaced key strata satisfy Eq. (4).

$$\frac{M_1}{E_1 I_1} = \frac{M_2}{E_2 I_2} = \frac{M_3}{E_3 I_3} \tag{4}$$

where E_1、E_2 和 E_3 are the elastic moduli of the high- position, middle- position, and low-position CDTHR, respectively, GPa；I_1、I_2 and I_3 are the vertical cross-sectional moments of inertia per unit thickness of the high- position, middle- position, and low-position CDTHR, respectively, m^2.

By simultaneously solving Eqs. (1) through (4), the analytical expressions for the supporting force F_1, the bending moment M_1 exerted by the adjacent rock mass on the high-position CDTHR, and the uniformly distributed load q_1 provided by the underlying strata to the high-position CDTHR during coal extraction are obtained, as expressed in Eqs. (5), (6), and (7).

$$F_1 = \frac{(q_0 l_2 E_1 h_1^2 - g\rho_1(E_2 h_2^2 + E_3 h_3^2)h_1 + q_0 l_2(E_2 h_2^2 + E_3 h_3^2))l_1}{(E_1 h_1^2 + E_2 h_2^2 + E_3 h_3^2)l_2}$$
$$+ \frac{E_1 g h_1^3 l_2 \rho_1 + E_1 h_1^2(g h_2 l_2 \rho_2 + g h_3 l_3 \rho_3) + g\rho_1 l_2(E_2 h_2^2 + E_3 h_3^2)h_1}{(E_1 h_1^2 + E_2 h_2^2 + E_3 h_3^2)l_2} \tag{5}$$
$$- \frac{q_0(E_2 h_2^2 + E_3 h_3^2)l_1^2}{(E_1 h_1^2 + E_2 h_2^2 + E_3 h_3^2)l_2}$$

$$M_1 = \frac{(g h_1 l_1 \rho_1 + g h_2 l_2 \rho_2 + g h_3 l_3 \rho_3 + l_1^2 q_0)E_1 h_1^2}{2E_1 h_1^2 + 2E_2 h_2^2 + 2E_3 h_3^2} \tag{6}$$

$$q_1 = \frac{-E_1 g(h_2 l_2 \rho_2 + h_3 l_3 \rho_3)h_1^2 + g\rho_1 l_1(E_2 h_2^2 + E_3 h_3^2)h_1 + q_0(E_2 h_2^2 + E_3 h_3^2)l_1^2}{(E_1 h_1^2 + E_2 h_2^2 + E_3 h_3^2)l_2^2} \tag{7}$$

Similarly, during coal extraction, the expressions for the supporting force F_2 and bending moment M_2 exerted by the adjacent rock mass on the middle-position CDTHR, as well as the uniformly distributed load q_2 provided by the underlying strata to the middle-position CDTHR, can be obtained, as expressed in Eqs. (8), (9), and (10).

$$F_2 = \frac{(E_3 l_3 \rho_2 g h_2 - E_3(g h_1 l_1 \rho_1 + l_1^2 q_0))h_3^2 - l_3 g\rho_3(-E_1 h_1^2 - E_2 h_2^2)h_3 + l_3 E_2 h_2^3 \rho_2 g}{(E_1 h_1^2 + E_2 h_2^2 + E_3 h_3^2)l_3}$$
$$+ \frac{E_3 l_3(g h_1 l_1 \rho_1 + l_1^2 q_0)h_3^2 - E_1 g h_1 2 h_3 l_3^2 \rho_3 + l_3 E_2 h_2^2(g h_1 l_1 \rho_1 + l_1^2 q_0)}{(E_1 h_1^2 + E_2 h_2^2 + E_3 h_3^2)l_3 l_2} \tag{8}$$
$$- \frac{l_2 E_3 g h_2 h_3^2 \rho_2}{(E_1 h_1^2 + E_2 h_2^2 + E_3 h_3^2)l_3}$$

$$M_2 = \frac{E_2 h_2^2(g h_1 l_1 \rho_1 + g h_2 l_2 \rho_2 + g h_3 l_3 \rho_3 + l_1^2 q_0)}{2E_1 h_1^2 + 2E_2 h_2^2 + 2E_3 h_3^2} \tag{9}$$

$$q_2 = \frac{h_3(-E_3((h_1 l_1 \rho_1 + h_2 l_2 \rho_2)g + q_0 l_1^2)h_3 + g l_3 \rho_3(E_1 h_1^2 + E_2 h_2^2))}{l_3^2(E_1 h_1^2 + E_2 h_2^2 + E_3 h_3^2)} \tag{10}$$

Concurrently, during coal extraction, the expressions for the supporting force F_3 and bending moment M_3 exerted by the adjacent rock mass on the low-position CDTHR (along with their associated parameters) are given in Eqs. (11), (12), and (13).

$$F_3 = \frac{h_3^3 E_3 \rho_3 g}{E_1 h_1^2 + E_2 h_2^2 + E_3 h_3^2} + \frac{h_3^2(g h_1 l_1 \rho_1 + g h_2 l_2 \rho_2 + l_1^2 q_0)E_3}{(E_1 h_1^2 + E_2 h_2^2 + E_3 h_3^2)l_3} \tag{11}$$

$$M_3 = \frac{E_3 h_3^2(g h_1 l_1 \rho_1 + g h_2 l_2 \rho_2 + g h_3 l_3 \rho_3 + l_1^2 q_0)}{2E_1 h_1^2 + 2E_2 h_2^2 + 2E_3 h_3^2} \tag{12}$$

As the coal mining advance distance increases, the load borne by the CDTHR the upper portion of the stope gradually increases. When the normal stress within the thick-hard roof reaches the maximum normal stress they can withstand, the working face roof

fractures. At this point, the normal stress acting on the key strata of the stope roof must satisfy the following expression:

$$\sigma = \frac{M}{W} \le [\sigma_{\max}] \tag{13}$$

where W is the section modulus of the key strata of the stope roof, $\sigma_{\max}$ is the maximum normal stress that the key strata of the stope roof can withstand, MPa.

Based on the above equation, by simultaneously solving Eqs. (6), (9), (12), and (13), the mechanical criteria for the ultimate load-bearing fracture and caving of the high- position, middle- position, and low-position CDTHR during coal extraction are expressed by Eqs. (14), (15), and (16), respectively:

$$q_{1\max} = \frac{(2E_1h_1^2 + 2E_2h_2^2 + 2E_3h_3^2)\sigma_{1\max}}{6E_1l_1^2} - \frac{gh_1l_1\rho_1 + gh_2l_2\rho_2 + gh_3l_3\rho_3}{l_1^2} \tag{14}$$

$$q_{2\max} = \frac{(2E_1h_1^2 + 2E_2h_2^2 + 2E_3h_3^2)\sigma_{2\max}}{6E_2l_1^2} - \frac{gh_1l_1\rho_1 + gh_2l_2\rho_2 + gh_3l_3\rho_3}{l_1^2} \tag{15}$$

$$q_{3\max} = \frac{(2E_1h_1^2 + 2E_2h_2^2 + 2E_3h_3^2)\sigma_{3\max}}{6E_3l_1^2} - \frac{gh_1l_1\rho_1 + gh_2l_2\rho_2 + gh_3l_3\rho_3}{l_1^2} \tag{16}$$

where $q_{1\max}$、$q_{2\max}$ and $q_{3\max}$ are the maximum external loads at the time of fracture for the high- position, middle- position, and low-position CDTHR during coal extraction, respectively, MPa; $\sigma_{1\max}$、$\sigma_{2\max}$ and $\sigma_{3\max}$ are the maximum normal stresses that the high- position, middle- position, and low-position CDTHR of the stope roof can withstand, respectively, MPa.

2.3 Evolutionary characteristics

Fig. 4 illustrates the evolutionary laws governing the combined load-bearing strength of stope roofs overlain by CDTHR. As observed, with an increase in the overhanging span of the CDTHR and a decrease in the maximum normal stress they can withstand, the ultimate load-bearing strength of the CDTHR in the stope roof progressively decreases. However, the ultimate load-bearing strength is more significantly sensitive to the overhanging span of the CDTHR. Specifically, an increase in the overhanging span leads to a substantially greater reduction in the ultimate load-bearing strength of the CDTHR, whereas a decrease in the maximum normal stress results in a distinctly smaller reduction. Furthermore, during coal extraction, the high-position CDTHR exerts the dominant influence on the overall load-bearing strength of the stope roof, followed by the middle-position key stratum, whereas the low-position key stratum exhibits the least influence.These distinct evolutionary influence laws governing the load-bearing characteristics of CDTHR dictate the sequential progressive fracturing of the stope roof during mining. In the initial stage of working face extraction, as the overhanging span of the stope roof gradually expands and roof stress undergoes continuous redistribution, the low-position CDTHR is the first to reach its ultimate load-bearing strength, undergoing combined tensile-shear failure and caving. At this

stage, the load borne by the high-position CDTHR remains below its ultimate load-bearing threshold; thus, it maintains a continuous structural integrity, ensuring the overall stability of the roof. As the working face advances continuously, the overhanging span of the roof expands further, accompanied by the persistent accumulation of external loads transferred from the overburden. Following the caving of the low-position CDTHR, the loads originally shared by the multi-layer CDTHR gradually transfer upward, causing a continuous rise in the force acting on the high-position CDTHR. When the accumulated load reaches the ultimate load-bearing strength of the high-position CDTHR, it undergoes structural fracturing and instability, ultimately triggering large-scale roof caving.

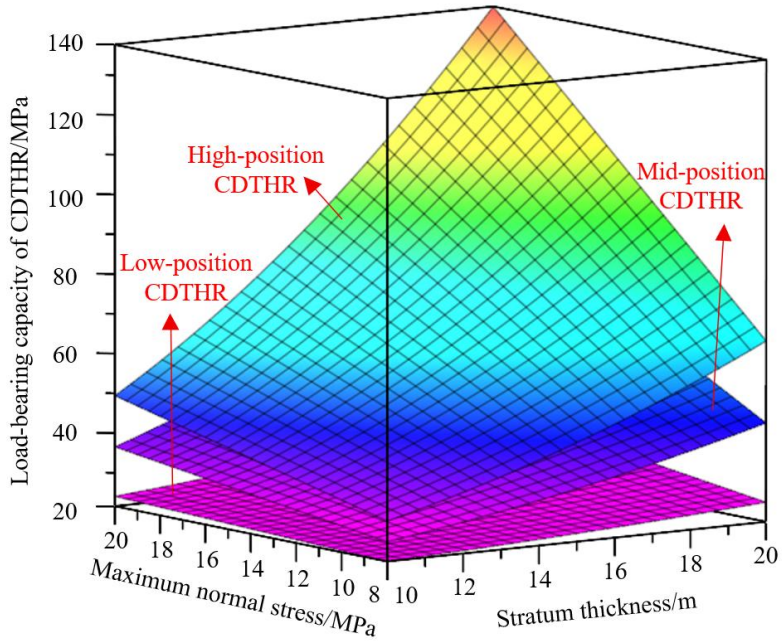

Fig. 4 Evolutionary laws of combined load-bearing strength for CDTHR

3 Physical similarity simulation of fracture-induced weakening for close distance thick-hard roofs

3.1 Experimental scheme

(1) Model construction

Based on the characteristics of the stope overburden and extraction parameters, and in accordance with similarity theory, a physical similarity model was constructed using an experimental platform with dimensions of 2500 mm × 200 mm × 1500 mm (length × width × height). The bulk density scale ratio and geometric similarity ratio of the model were set to 1.667 and 1:100, respectively. A total of 23 strata were simulated within the model. All strata utilized quartz sand with a median particle size of 0.25 mm as the overburden aggregate, bonded with lime and gypsum cementing materials. Additionally, mica flakes with a thickness of 0.2 mm and a diameter of 20 mm were uniformly placed between adjacent strata to simulate the bedding planes of the overburden. The mix proportion parameters for each stratum in the model are listed in Table 1. Furthermore, stationary pneumatic pumps positioned at the top and both lateral

sides of the experimental platform were used to apply a vertical stress of 26.19 kPa and a lateral stress of 20.95 kPa, respectively, to simulate the in-situ stress environment of the stope.

Table 1 Mix proportions of coal and rock strata in the physical similarity model

No.	Lithology	Simulated thickness /cm	Simulated strength kPa	Sand /kg	Lime /kg	Gypsum /kg	Water /kg
R20	Shale	6.78	32.36	81.57	5.83	5.83	81.57
R19	Mudstone	4.74	28.40	55.86	6.52	2.79	55.86
R18	Coarse-grained sandstone	3.93	198.47	45.03	2.70	6.30	45.03
R17	Limestone	5.69	102.85	62.59	4.69	10.95	62.59
R16	Fine-grained sandstone	4.21	181.26	49.62	2.48	5.79	49.62
R15	Shale	3.93	32.36	47.28	3.38	3.38	47.28
R14	Mudstone	5.42	28.40	63.88	7.45	3.19	63.88
R13	Medium-grained sandstone	6.48	169.48	71.28	8.91	8.91	71.28
R12	Shale	8.17	32.36	98.30	7.02	7.02	98.30
R11	Fine-grained sandstone	8.82	181.26	103.95	5.20	12.13	103.95
R10	Mudstone	3.75	28.40	44.20	5.16	2.21	44.20
R9	Medium-grained sandstone	12.62	169.48	138.82	17.35	17.35	138.82
R8	Shale	6.09	32.36	73.27	5.23	5.23	73.27
R7	Coarse-grained sandstone	11.53	198.47	132.11	7.93	18.50	132.11
R6	Mudstone	3.41	28.40	40.19	4.69	2.01	40.19
R5	Fine-grained sandstone	5.25	181.26	61.88	3.09	7.22	61.88
R4	Shale	4.09	32.36	49.21	3.51	3.51	49.21
R3	Fine-grained sandstone	11.79	181.26	138.95	6.95	16.21	138.95
R2	Mudstone	4.1	28.40	48.32	5.64	2.42	48.32
R1	Shale	2.41	32.36	29.00	2.07	2.07	29.00
C	Coal	7.44	52.04	85.25	11.94	5.12	85.25
F1	Mudstone	3.37	28.40	39.72	4.63	1.99	39.72
F2	Limestone	5.98	102.85	65.78	4.93	11.51	65.78

(2) Fracturing and excavation

To eliminate boundary effects, the mining stope was positioned in the middle of the model, with boundary coal pillars of 45 cm reserved on both the left and right sides of the excavation zone. The model was excavated sequentially from left to right with a single excavation step length of 6.0 cm and an interval time of 30 min per step, continuing until the total excavation length reached 160 cm, at which point the simulation was completed.

To simulate the fracturing cracks, high-density expanded polystyrene (EPS) foam boards with a thickness of 1 cm were pre-embedded within the model. Specifically, for the low-position CDTHR located at 12.41 cm above the coal seam roof, foam boards with a length of 53.48 cm were continuously laid starting from 79.46 cm to the right of the model's left side; for the middle-position CDTHR located at 36.82 cm above the

coal seam roof, foam boards with a length of 77.43 cm were continuously laid starting from 70.52 cm to the right of the model's left side; and for the high-position CDTHR located at 54.98 cm above the coal seam roof, foam boards with a length of 77.43 cm were continuously laid starting from 70.52 cm to the right of the model's left side. Prior to model excavation, a specialized resistive thermal cutter was used to melt the foam boards to simulate the fracture-induced cracks in the CDTHR, after which the model was excavated in accordance with the prescribed excavation steps.

(3) Monitoring scheme

To monitor the displacement laws of the CDTHR during the excavation process, white latex paint was first evenly coated on the surface of the model. Once the white latex paint was completely dried, measurement lines(MLs) were laid out along both the horizontal and vertical directions at 10 cm × 10 cm intervals. The MLs located above the coal seam roof were designated sequentially from bottom to top as ML 1 to ML 12. Meanwhile, a Portable Paladin 5 micro-seismic (MS) monitoring system was employed, utilizing a Paladin digital recorder for signal acquisition. Professional post-processing software was then used to monitor the magnitude of released energy, occurrence frequency, and failure locations during the overburden fracture process induced by model excavation. A total of 7 MS sensors were installed within the model: sensors No. 1, No. 2, and No. 3 were positioned 30 cm from the right side of the model, at distances of 10 cm, 60 cm, and 110 cm above the coal seam roof, respectively; sensors No. 5, No. 6, and No. 7 were positioned 30 cm from the left side of the model, at distances of 110 cm, 60 cm, and 10 cm above the coal seam roof, respectively; and sensor No. 4 was placed in the exact center of the model at 10 cm from the top. The fracture-induced weakening model for CDTHR in shallow thick coal seams is illustrated in Fig. 5.

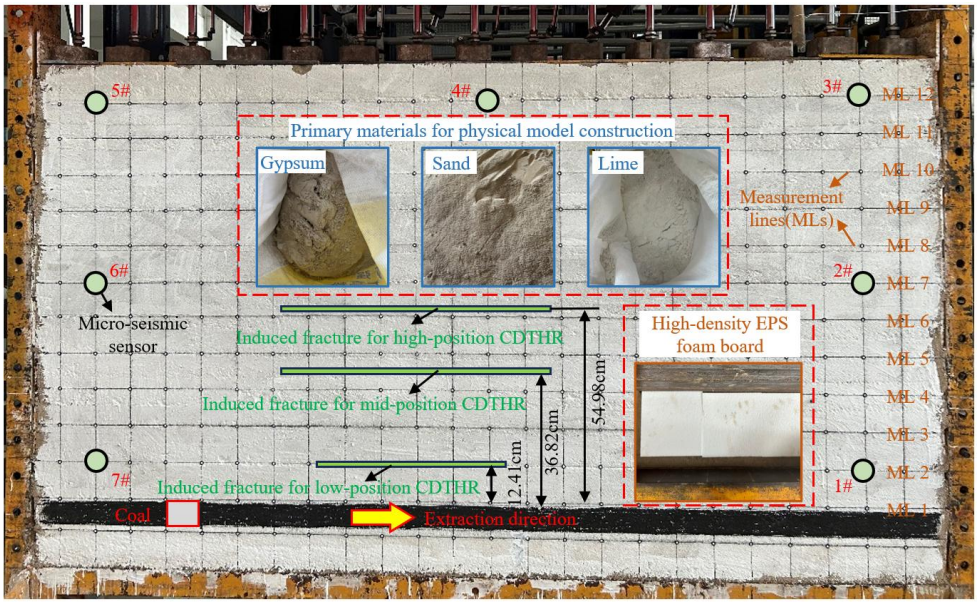

Fig. 5 Fracture-induced weakening model and monitoring scheme for CDTHR

3.2 Fracture and caving characteristics

Fig. 6 illustrates the fracture and caving configurations of the CDTHR subjected to fracture-induced weakening under different mining stages. As the working face

advances continuously, the fracture and caving process of the weakened competent key strata in the stope roof can be divided into four distinct stages: 'initial localized fracture - staged advanced fracture - slow progressive fracture - multi-layer cooperative fracture'.

(1) When the working face advances to 40 m, the immediate roof of the stope first undergoes initial localized fracturing and caving. At this point, even though the competent key strata remain in an overhanging state, their strong load-bearing characteristics prevent any significant damage to the strata overlying the coal seam.

(2) At a retreat distance of 80 m, the caving range of the immediate roof increases significantly, while the low-position competent key stratum and the middle-position key stratum experience their initial fracturing and caving phenomena due to the fracture-induced weakening effect. The fractured and caved blocks exhibit prominent articulated locking characteristics within the goaf. Furthermore, following the caving of the low-position competent key stratum, an overhanging triangular zone forms on the coal wall side of the goaf within the roof strata, where the angle between the roof fracture line and the horizontal plane is 78°. Influenced by the fracturing cracks, an advanced overhanging triangular zone appears on the extraction side of the goaf within the roof strata, with a fracture line-to-horizontal plane angle of 64°.

(3) Upon advancing the working face to 120 m, the roof fracture range extends further along the mining direction. In this stage, influenced by the fracture-induced weakening of the middle-position key stratum, the low-position competent key stratum exhibits slow, progressive fracturing and caving characteristics as the working face advances. The dimensions of the fractured and caved roof blocks decrease markedly. Concurrently, the advanced overhanging triangular zone formed ahead of the working face after the initial fracture gradually disappears, being replaced by an overhanging triangular zone lagging behind the working face, where the angle between the roof fracture line and the horizontal plane is 44°.

(4) During the process of the working face advancing to 160 m, the stope roof fracture range increases remarkably in both horizontal and vertical directions. At this juncture, the low-, middle-, and high-position competent key strata undergo multi-layer cooperative fracturing and caving. During this stage, the size of the fractured and caved blocks in the low-position competent key stratum is the smallest, followed by the middle-position competent key stratum, while the high-position competent key stratum exhibits the largest blocks. Moreover, after the caving of the competent key strata, overhanging triangular zones form on both the coal wall side and the extraction side of the roof strata. The range of the overhanging triangular zone on the coal wall side is significantly smaller than that on the extraction side, with the angles between their respective roof fracture lines and the horizontal plane being 52° and 74°, respectively.

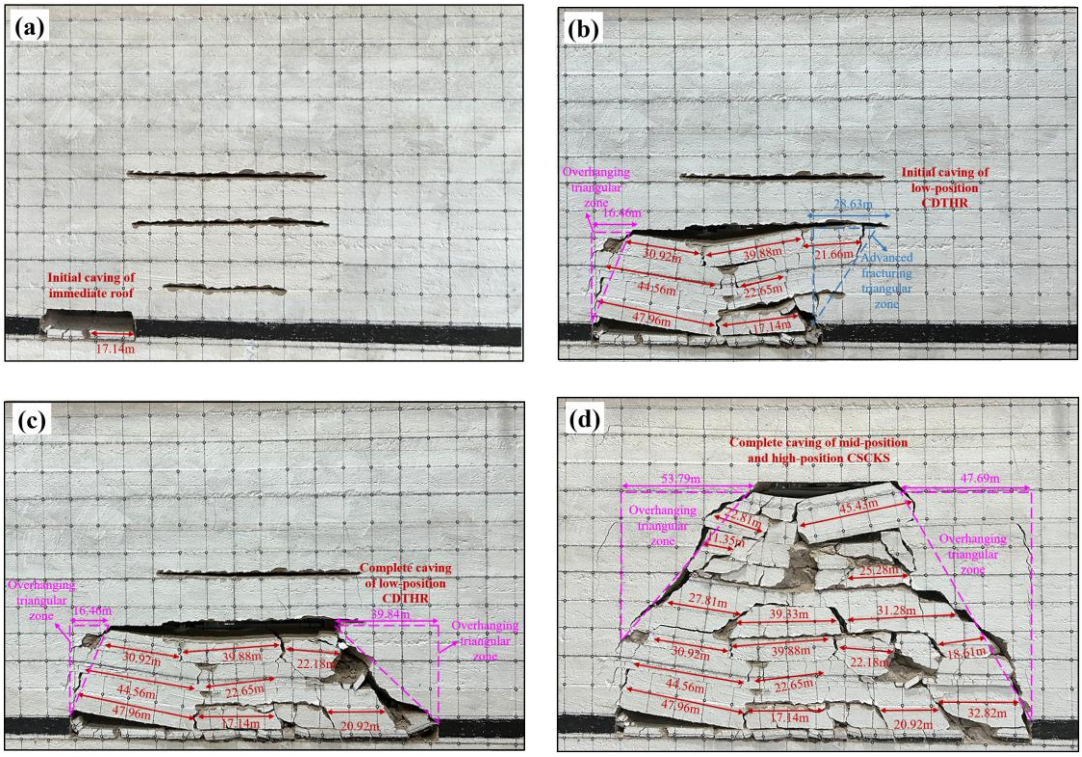

Fig. 6 Fracture and caving morphologies of CDTHR subjected to fracture-induced weakening under different mining stages: (a) 40 m; (b) 80 m; (c) 120 m; (d) 160 m.

Fig. 7 illustrates the schematic sketches of the CDTHR subjected to fracture-induced weakening under different mining stages. As the working face advances, the fracture range of the weakened stope roof gradually expands, exhibiting a predominantly trapezoidal profile. Concurrently, under mining-induced effects, both the number and length of fractures within the coal seam overburden increase significantly.

(1) When the working face advances to 40 m, the immediate roof of the coal seam undergoes its initial fracture and caving. Due to the limited mining extent and the strong load-bearing characteristics of the CDTHR, the roof caving range remains below the low-position CDTHR under this stage. The mining-affected stope roof region constitutes the caving zone, with lower and upper lengths of 37.13 m and 31.61 m, respectively, and an overall influence height of 11.49 m.

(2) At a retreat distance of 80 m, the low-position CDTHR undergoes distinct fracture and caving, accompanied by partial fracturing of the middle-position CDTHR. The stope roof caving range extends above the low-position CDTHR but remains below the middle-position CDTHR. The mining-affected stope roof regions comprise the caving zone, fractured zone, and separation zone. Specifically, the lower and upper lengths of the caving zone are 88.83 m and 95.07 m, respectively, with an overall influence height of 35.87 m; the lower and upper lengths of the fractured zone are 107.52 m and 91.37 m, respectively, with an overall influence height of 39.02 m; and the lower and upper lengths of the separation zone are 75.44 m and 24.03 m, respectively, with an overall influence height of 13.58 m.

(3) Upon advancing the working face to 120 m, the fracture and caving range of the low-position CDTHR and partial middle-position CDTHR increases remarkably. The primary caving range remains concentrated between the low- position and middle-position CDTHR, whereas the high-position CDTHR maintains favorable integrity and load-bearing capacity. Consequently, the mining-affected stope roof region under this stage is mainly distributed below the fractured zone of the middle-position CDTHR, while the region above it experiences minimal mining-induced influence. The lower and upper lengths of the caving zone increase to 144.91 m and 98.69 m, respectively, with the overall influence height increasing significantly to 39.41 m, whereas the ranges of the fractured and separation zones exhibit minor changes.

(4) During the process of the working face advancing to 160 m, the low- position, middle- position, and high-position CDTHR undergo multi-layer cooperative fracturing. Because the high-position CDTHR suffers severe damage and fails to provide effective support for the overlying strata, multiple overlying strata layers experience joint fracturing and caving. At this point, the stope roof caving range extends far above the high-position CDTHR. The mining-affected stope roof region is characterized by an expanded caving zone, with lower and upper lengths of 164.33 m and 66.51 m, respectively, and an overall influence height of 103.22 m.

Overall, due to their substantial thickness and robust load-bearing characteristics, CDTHR play a core role in the strata overlying the coal seam. During coal extraction, as long as the CDTHR remain unfractured, the multiple strata layers above them receive effective support, preventing significant damage. However, once the CDTHR exceed their load-bearing limit and fracture, the overlying multi-layer CDTHR undergo simultaneous fracturing and caving. Therefore, implementing fracture-induced weakening on CDTHR can effectively disrupt their integrity, reduce their load-bearing capacity, eliminate long-distance roof hanging phenomena, and force them to fracture and cave progressively with the advancement of the working face.

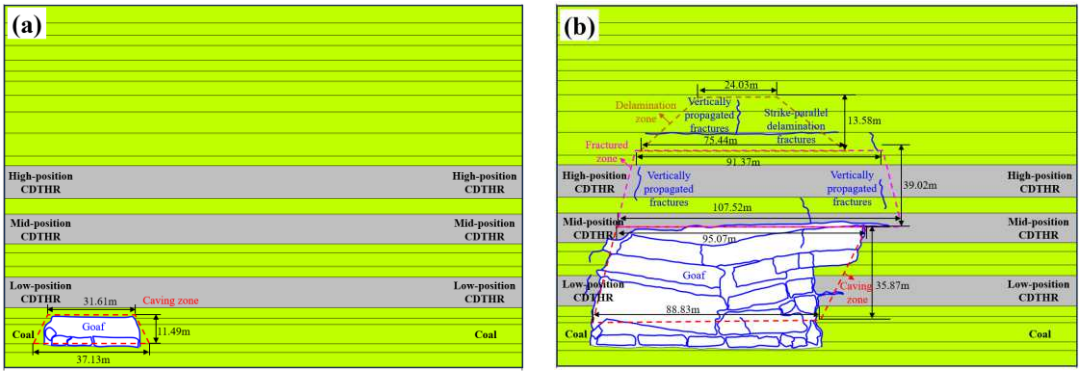

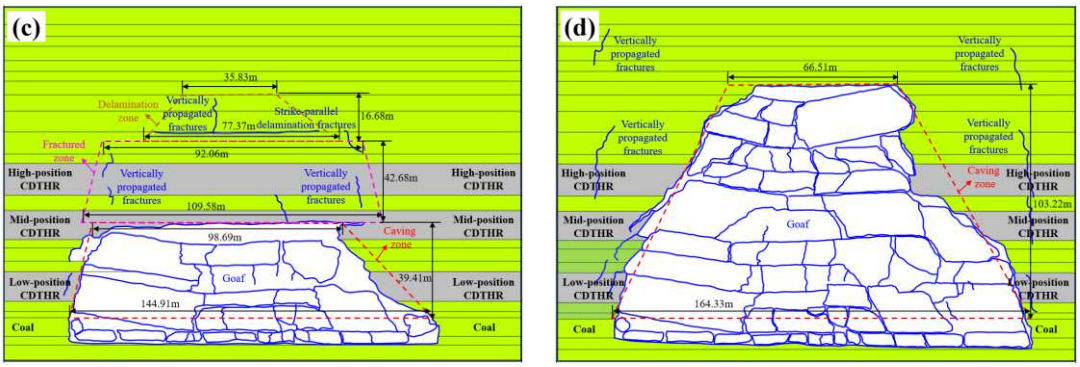

Fig. 7 Schematic sketches of CDTHR subjected to fracture-induced weakening under different mining stages: (a) 40 m; (b) 80 m; (c) 120 m; (d) 160 m

3.3 Displacement evolution laws

Fig. 8 illustrates the displacement contour maps of the CDTHR subjected to fracture-induced weakening under different mining stages. As the working face advances, the mining-affected range of the CDTHR increases continuously, evolving from a 'localized single-wing disturbance' to a 'large-scale, high-displacement disturbance'.

(1) When the working face advances to 40 m, the mining disturbance has a minor impact on the stope overburden. The mining-affected region within the CDTHR is primarily concentrated within a small scope in the middle of the immediate roof, exhibiting a narrow strip-like profile along the horizontal direction. At this stage, the mining disturbance does not affect the CDTHR, which maintain favorable load-bearing characteristics.

(2) At a retreat distance of 80 m, the mining-affected range within the stope roof expands significantly in both horizontal and vertical directions. Vertically, the mining-affected zone extends into the middle-position CDTHR. The core displacement region of the coal seam roof is located on the extraction side of the goaf, where the roof undergoes fracture and caving due to mining disturbance, resulting in large rock displacements. Furthermore, the maximum mining-induced displacement of the CDTHR increases from 7.44 cm to 7.72 cm, showing a notable increment.

(3) Upon advancing the working face to 120 m, the mining-affected range within the CDTHR further expands horizontally and vertically; however, it remains predominantly concentrated below the middle-position CDTHR. This indicates that the mining disturbance exerts a substantial influence on the low-position and middle-position CDTHR, whereas the high-position CDTHR remains unaffected by the working face advance. Concurrently, the core displacement region of the CDTHR shifts to the coal wall side of the goaf, while portions of the CDTHR on the extraction side exhibit relatively large displacements but within a narrower range.

(4) During the process of the working face advancing to 160 m, the mining-affected range of the CDTHR reaches its maximum. The affected region expands further horizontally and progressively propagates upward vertically, ultimately breaching the high-position CDTHR. At this juncture, the influence of the working face

mining disturbance on stope roof displacement exhibits a dual-core distribution characteristic: a horizontal strip-like displacement center located below the low-position CDTHR and an inclined funnel-shaped displacement center situated in the middle of the high-position CDTHR. Simultaneously, the mining-induced displacement of the CDTHR attains a maximum value of 8.46 cm.

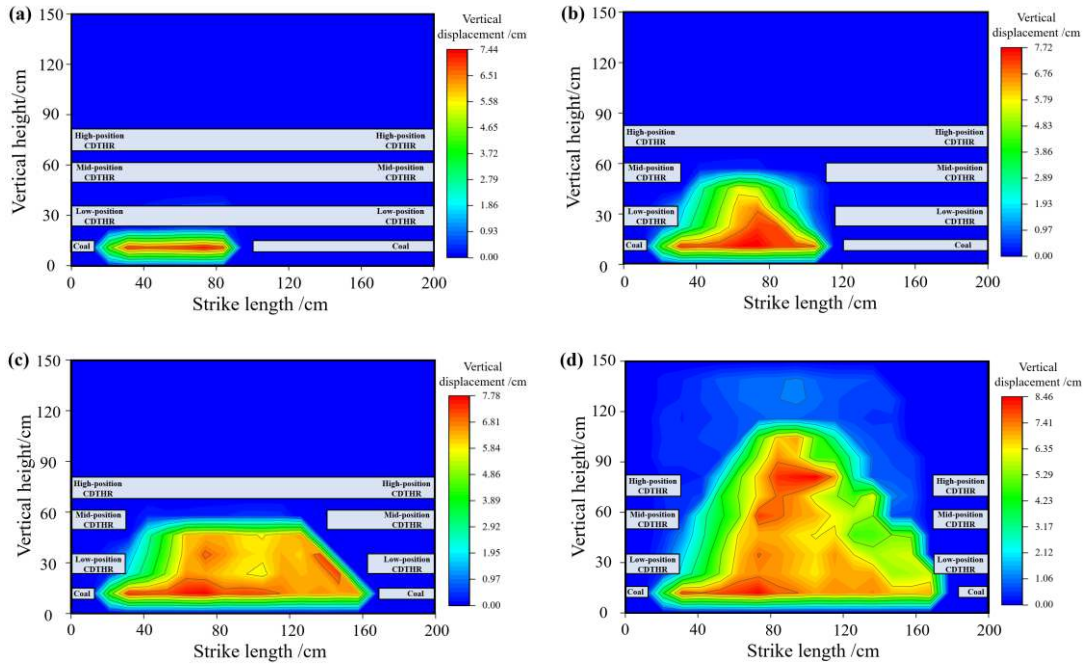

Fig. 8 displacement contour map of CDTHR subjected to fracture-induced weakening under different mining stages: (a) 40 m; (b) 80 m; (c) 120 m; (d) 160 m

Fig. 9 presents the displacement evolution laws of the CDTHR subjected to fracture-induced weakening under different mining stages. As the working face advances, the displacement evolution behavior of the CDTHR transitions from localized single settlement to large-scale cooperative subsidence.

(1) When the working face advances to 40 m, the overall displacement of the CDTHR is relatively small. Aside from prominent subsidence in the immediate roof of the coal seam, the roof remains stable across most areas. Owing to the high strength of the coal seam roof, no significant bending subsidence occurs during its load-bearing stage; however, once its load-bearing strength exceeds its capacity, the stope roof undergoes sudden fracture subsidence, characterized by abrupt displacement drops and steep inclination angles on both sides of the curve.

(2) At a retreat distance of 80 m, the immediate roof of the stope continues to subside, while the low-position and middle-position CDTHR undergo cooperative fracture subsidence. This fracture subsidence process is relatively intense, with steep inclination angles on both flanks of the displacement curve.

(3) Upon advancing the working face to 120 m, the displacement range of the CDTHR increases remarkably. Concurrently, the low-position and middle-position CDTHR experience 'exfoliation-style' cooperative fracture subsidence, causing the displacement curve on the extraction side of the goaf to appear nearly vertical. This

indicates that the fracture subsidence of the CDTHR is relatively intense. In addition, the strata overlying the middle-position CDTHR exhibit bending subsidence, with a maximum bending subsidence displacement of 0.57 cm.

(4) During the process of the working face advancing to 160 m, the CDTHR displacement curve displays more complex fluctuation characteristics overall. At this stage, the low-position, middle-position, and high-position CDTHR all undergo fracture subsidence, accompanied by simultaneous fracture subsidence in partial strata overlying the high-position CDTHR. Due to the fracture and caving of the high-position CDTHR, the overlying strata lose effective support and fracture accordingly, creating a large-scale void. This drives significant bending subsidence across multiple strata layers in a higher zone, with the maximum bending subsidence displacement reaching 1.27 cm.

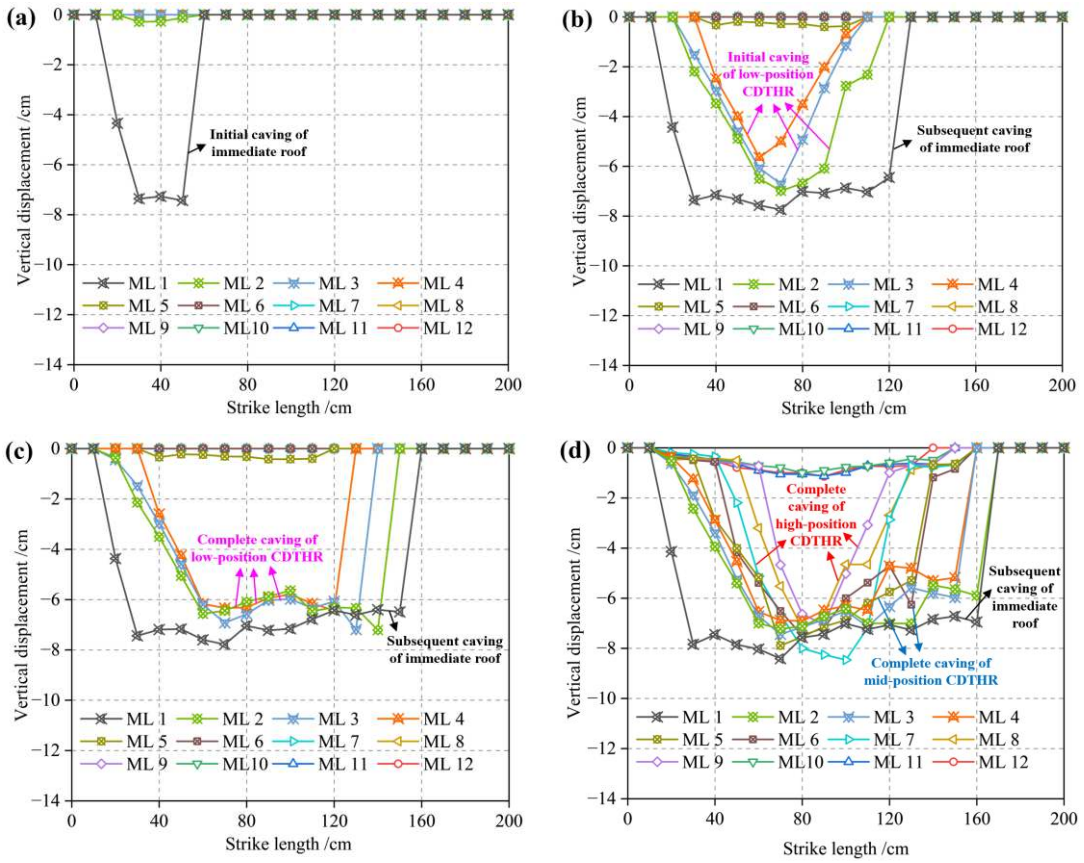

Fig. 9 Displacement evolution laws of CDTHR subjected to fracture-induced weakening under different mining stages: (a) 40 m; (b) 80 m; (c) 120 m; (d) 160 m

3.4 Micro-seismic event

Fig. 10 displays the micro-seismic (MS) contour maps of CDTHR subjected to fracture-induced weakening under different mining stages.

(1) During the process of the working face advancing to 40 m, the frequency of micro-seismic events occurring within the stope overburden is relatively low, and these events are primarily concentrated in the mined coal seam and its immediate roof. Although a few micro-seismic events appear within the low-position CDTHR, the energy released in this region is generally low. At this stage, the mining disturbance

primarily affects the roof between the coal seam and the low-position CDTHR while exerting minimal influence on the low-position CDTHR itself, which largely maintains favorable stability.

(2) At a retreat distance of 80 m, the range of micro-seismic events within the stope overburden expands significantly in both horizontal and vertical directions, accompanied by a marked increase in the frequency and energy of these events. At this juncture, the micro-seismic events are mainly concentrated in the low- position and middle-position CDTHR, indicating that the elastic energy of the rock strata induced by mining disturbance is predominantly stored within the CDTHR. When the CDTHR fracture and cave, the elastic energy stored internally is released outward, readily triggering ground pressure bumps. Furthermore, because the pre-formed fracturing cracks segment the middle-position CDTHR, the lower portion of the middle-position CDTHR fractures first, releasing partial energy via micro-seismic events and thereby substantially mitigating the impact shock generated during CDTHR fracture and caving.

(3) Upon advancing the working face to 120 m, the spatial range of micro-seismic events within the stope overburden expands mainly along the horizontal direction, whereas the event frequency decreases remarkably, and the released energy exhibits only a minor increase. This is because the fracturing cracks partition the middle-position CDTHR, confining the working face mining influence primarily between the coal seam and the fractured zone of the middle-position CDTHR, where the micro-seismic events are predominantly concentrated.

(4) During the process of the working face advancing to 160 m, the range of micro-seismic events within the stope overburden increases noticeably along the vertical direction, with significant enhancements in both event frequency and released energy. In addition, because the fracturing cracks weaken the load-bearing capacity of the high-position CDTHR, the mining influence of the working face propagates into multiple strata layers above the high-position CDTHR, thereby inducing a large number of micro-seismic events in this region. However, the zones within the overburden releasing higher micro-seismic energy remain localized within the high-position CDTHR.

In summary, the CDTHR in the upper portion of the stope serve as the primary regions for storing elastic energy induced by working face mining disturbances. When the upper CDTHR reach their strength limits and undergo failure, the massive amount of accumulated internal elastic energy is released, which can easily induce intense strata behavior and rock bursts. Moreover, utilizing fracturing cracks to rationally segment CDTHR, thereby disrupting their integrity and weakening their load-bearing capacity to ensure the orderly release of energy accumulated within the CDTHR, represents an effective approach for mitigating mine pressure hazards and strata impact threats.

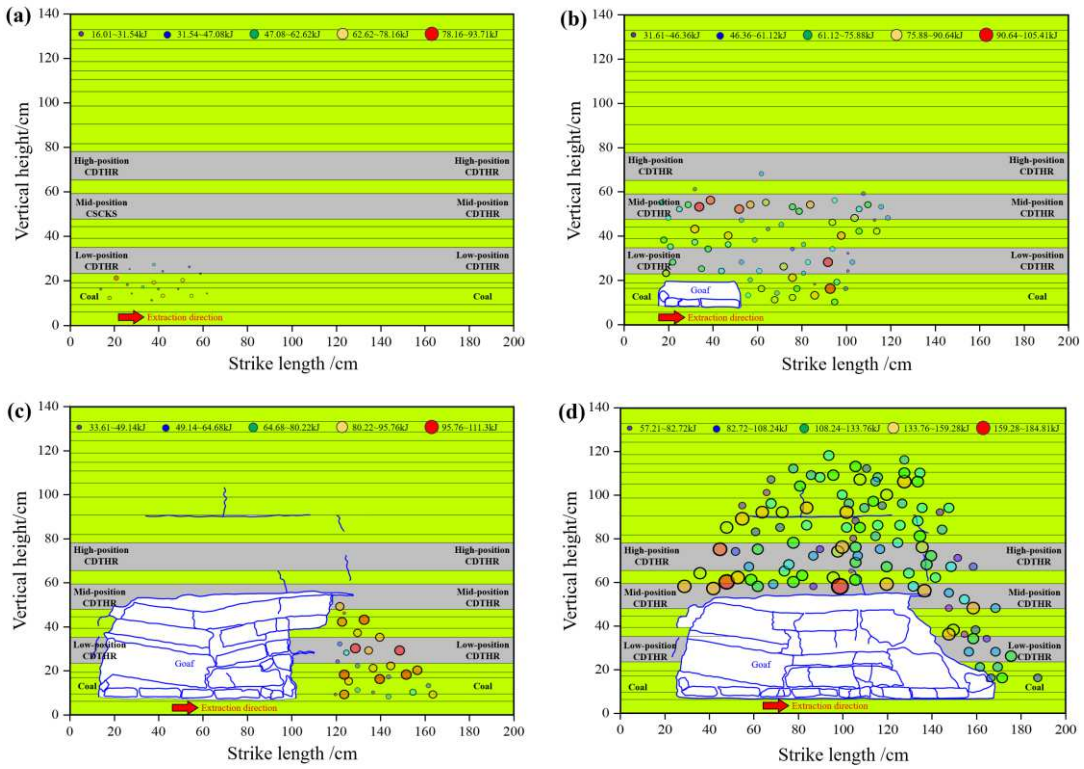

Fig. 10 Micro-seismic (MS) contour maps of CDTHR subjected to fracture-induced weakening under different mining stages: (a) 40 m; (b) 80 m; (c) 120 m; (d) 160 m

4 Field application of fracture-induced weakening for close distance thick-hard roofs

4.1 Technical scheme

To effectively mitigate strata pressure in the working face, segmented directional long-borehole hydraulic fracturing technology was adopted to fracture and weaken the CDTHR of the stope. Fracturing boreholes for the high-position, middle-position, and low-position CDTHR were arranged sequentially from bottom to top. Considering that the surrounding rock of the haulage roadway in the 31108 working face is in a better control condition, the drilling rigs for the high-position and middle-position CDTHR fracturing boreholes were set up within the haulage roadway of the 31108 working face to minimize the impact of CDTHR weakening on mining operations, while the drilling rig for the low-position CDTHR fracturing borehole was installed in the haulage roadway of the 31106 working face. The layout of the roof fracturing and weakening boreholes of the CDTHR is illustrated in Fig. 11. The borehole parameters for the high-position, middle-position and low-position CDTHR are designed as follows:

(1) The borehole for the high-position CDTHR is drilled from the haulage roadway of the 31108 working face toward the 31106 working face, with an opening angle of 66°, an inclined section length of 109.17 m, a horizontal section length of 75.82 m, a total borehole length of 184.99 m, and a terminal vertical height of 54.98 m.

(2) The borehole for the middle-position CDTHR is drilled from the haulage roadway of the 31108 working face toward the 31106 working face, with an opening

angle of 57°, an inclined section length of 83.04 m, a horizontal section length of 92.58 m, a total borehole length of 175.62 m, and a terminal vertical height of 36.82 m.

(3) The borehole for the low-position CDTHR is drilled from the haulage roadway of the 31106 working face toward the 31106 working face, with an opening angle of 37°, an inclined section length of 42.62 m, a horizontal section length of 67.88 m, a total borehole length of 110.50 m, and a terminal vertical height of 12.41 m.

During borehole construction, the inclined section was drilled at a preset inclination angle. Upon reaching the target CDTHR height, the drilling trajectory was adjusted to maintain a nearly horizontal extension along the interior of the CDTHR. The trajectory of the inclined borehole section adopted a large-radius smooth circular arc transition, controlling the tangential rotation angle per meter of arc length to less than 6° to minimize directional drilling friction, ensure smooth borehole profiles, and reduce the operational difficulty of borehole sealing and high-pressure hydraulic fracturing.

Upon completion of borehole construction, a staged sealing and step-by-step hydraulic fracturing technique was implemented on the CDTHR. First, a downhole borehole televiewer was utilized to inspect fracture development along the borehole wall, filtering out defective sections prone to hole collapse or diameter shrinkage. Next, inflatable rubber packers were employed to isolate target intervals within the CDTHR, establishing independent fracturing chambers. Finally, a high-pressure pump was activated to raise the water pressure incrementally, utilizing high-pressure water to dilate pre-existing rock fractures and generate new radial cracks. This formed an interconnected fracture network, thereby weakening the integrity of the CDTHR.

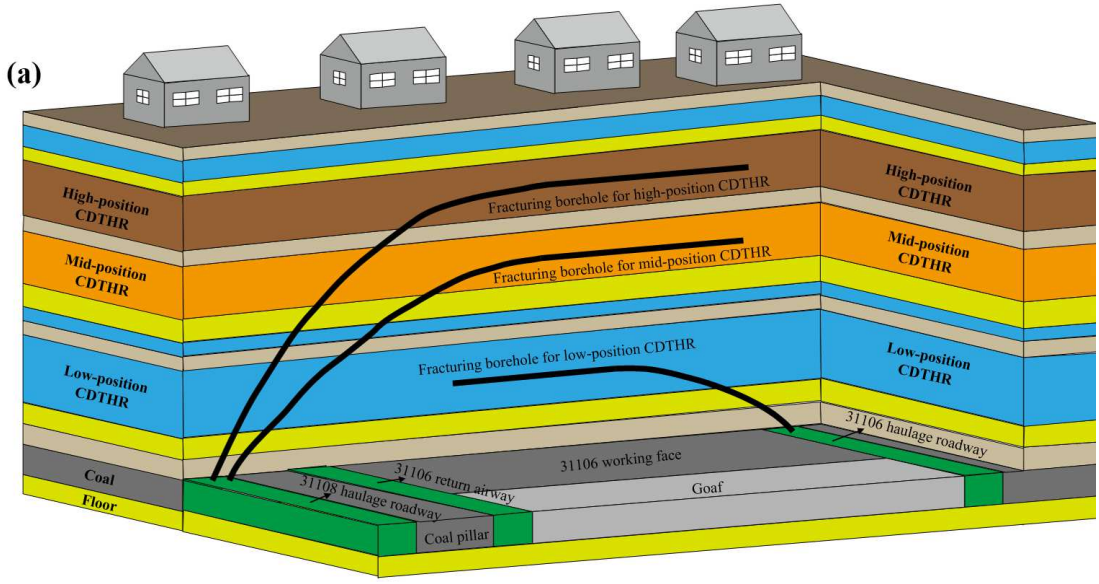

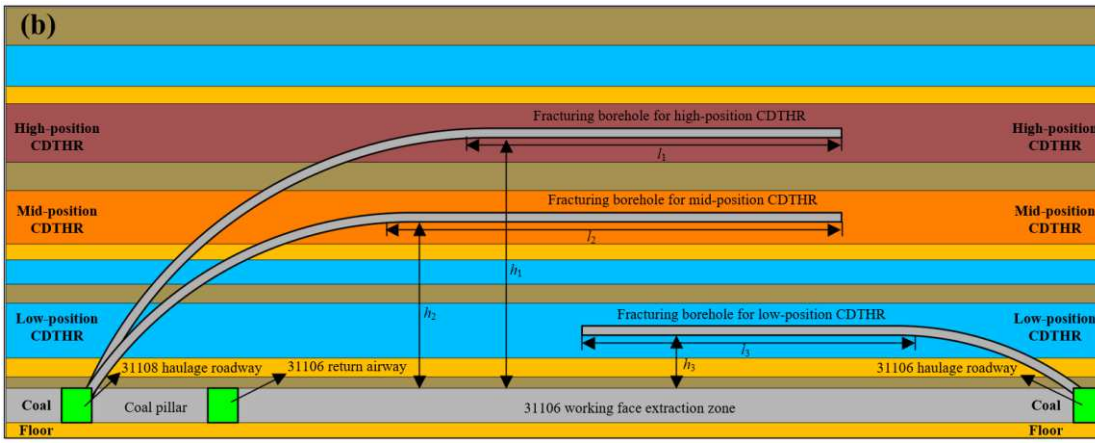

642 Fig. 11 Technical scheme for fracture-induced weakening of CDTHR: (a) 3D layout of fracturing
643 boreholes; (b) profile layout of fracturing boreholes.

644 **4.2 Evolution laws of fracturing pressure**

645 Fig. 12 illustrates the evolution laws of water injection pressure and total water
646 injection volume during the fracture-induced weakening of CDTHR in the stope. Based
647 on the analysis, the fracture-induced weakening process of the CDTHR in the stope can
648 be divided into four stages: initial fluid-filling stage, initial fracture propagation stage,
649 periodic fracturing stage, and pressure-relief stage.

650 (1) Initial fluid-filling stage (approximately 0 ~ 12 min): The total water injection
651 volume increases approximately linearly with time, while the water injection pressure
652 rises slowly. At this stage, high-pressure water is primarily used to fill the borehole,
653 pipelines, and primary pores of the CDTHR, and has not yet reached the fracture
654 initiation threshold of the CDTHR. With continuous pumping, the water pressure inside
655 the borehole accumulates. When the injection pressure reaches the CDTHR failure
656 strength, the rock mass begins to crack, entering the initial fracture propagation stage,
657 during which the injection pressure reaches its maximum value of 35.97 MPa.

658 (2) Initial fracture propagation stage (12min ~ 18 min): The injection pressure
659 rapidly rises to a peak and then drops sharply. At this point, the injection pressure
660 quickly ascends to the fracture initiation pressure of the rock mass, inducing tensile
661 failure at the tips of the primary fractures within the CDTHR. This causes the newly
662 formed fractures to open and propagate instantaneously, resulting in a sudden increase
663 in fluid volume after fracture formation and the rapid release of borehole injection
664 pressure, thereby producing a prominent pressure drop. Following the initial fracture
665 completion, the fractures are not fully connected; as fluid continues to be pumped, the
666 pressure recovers and enters an oscillatory range.

667 (3) Periodic fracturing stage (18 min ~ 60 min): This represents the primary stage
668 of fracture-induced weakening for the CDTHR. The total water injection volume
669 continues to increase linearly, while the injection pressure maintains continuous
670 reciprocal oscillation within the range of 22MPa - 30 MPa, exhibiting distinct periodic
671 fluctuation characteristics. After the initial fractures form, the fracture surfaces partially
672 close under the action of in-situ stress, causing the injection pressure to accumulate

once again. When the injection pressure reaches the rock failure strength for the second time, the fractures undergo secondary propagation, and the pressure drops again, repeating in this cyclic manner. The up-and-down oscillations of the injection pressure during this process represent the periodic cycle of fracture 'pressure accumulation - propagation - pressure relief'. Each peak of the injection pressure corresponds to the initiation and propagation of a fracture, whereas each valley corresponds to stress release following fracture propagation. Concurrently, the sustained fluctuations in injection pressure indicate that the hydraulic fractures continuously initiate and propagate within the CDTHR, during which internal damage continuously accumulates, progressively forming a complex fracture network.

(4) Pressure-relief stage (after 60 min): Following the cessation of water injection, the total water injection volume ceases to increase, and the injection pressure drops rapidly to 0 MPa. At this juncture, the high-pressure water within the fractures continues to seep and discharge along the fractures, causing the borehole water pressure to dissipate quickly, and the CDTHR fractures gradually tend to close under the action of surrounding rock stress.

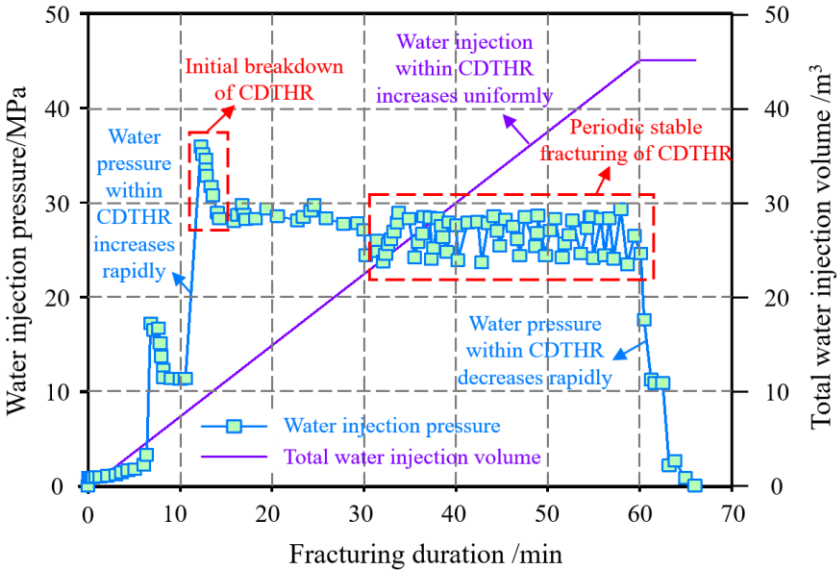

Fig. 12 Evolution laws of water injection pressure and total water injection volume during the fracture-induced weakening of stope roofs in closely spaced key strata.

4.3 Distribution characteristics of working face support resistance

Fig. 13 displays the contour maps of working face support resistance before and after the fracture-induced weakening of CDTHR in the stope. As observed, prior to the fracturing of the CDTHR, the stope roof exhibits three periodic weighting characteristics during working face extraction. Specifically, the initial weighting of the stope occurs at a mining advance of approximately 50 m, where the working face support resistance is relatively high, forming a continuous high-resistance strip along the dip direction. This indicates that the CDTHR undergoes a large-scale, one-off fracture, releasing concentrated energy. The secondary weighting of the stope occurs near a mining advance of 150 m, with a weighting step interval of 95.46 m between the

initial and secondary weightings. The third weighting of the stope occurs around a mining advance of 300 m, with the step interval between the secondary and third weightings reaching 148.53 m. Overall, prior to the fracturing of the CDTHR, the periodic weighting step interval of the stope roof is relatively large, accompanied by high working face support resistance during weighting, with the maximum support resistance reaching up to 62.44 MPa. Furthermore, the high support resistance strips are continuous and concentrated during working face weighting, indicating that the CDTHR struggles to cave in a timely manner after becoming overhanging, and that long-distance overhanging plate structures accumulate a massive amount of elastic energy. Once fractured, the working face experiences intense strata behavior, and large weighting step intervals increase the risk of rock bursts in the working face, which is unfavorable for stope surrounding rock control.

In contrast, after the fracture-induced weakening of the CDTHR, the stope roof experiences four periodic weighting phenomena during working face extraction, with weighting step intervals of 52.43 m, 76.94 m, and 64.31 m, respectively. Compared with the period prior to CDTHR, the periodic weighting step intervals of the stope roof during working face extraction are significantly shortened, and the respective weighting step intervals become more uniform. Simultaneously, the working face support resistance is remarkably reduced, with its maximum resistance dropping to 48.59 MPa. In addition, the continuity of the high support resistance strips during working face weighting is weakened, and the degree of stress concentration is alleviated. This demonstrates that following fracture-induced weakening of the CDTHR, artificial weak planes are formed within the rock strata, prematurely weakening roof integrity and transforming the original large-area, one-off plate-like roof fracture pattern into segmented, multi-stage, small-scale roof fracture patterns.

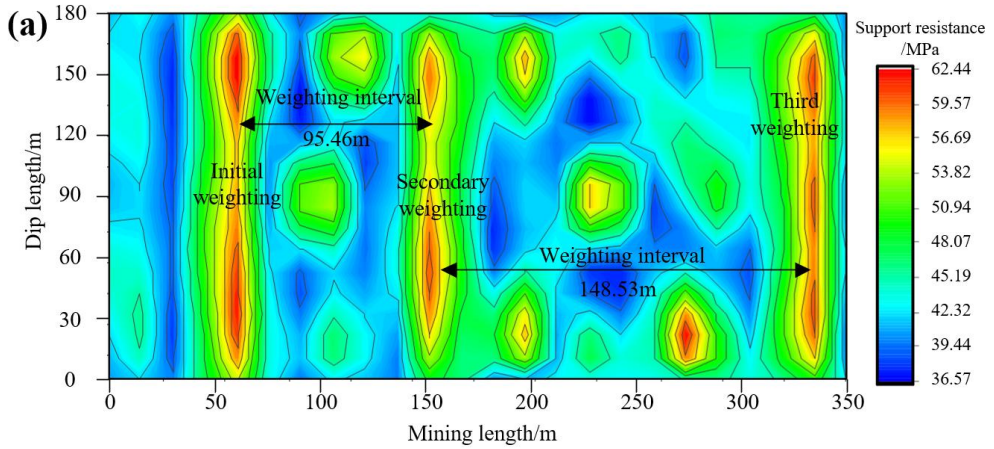

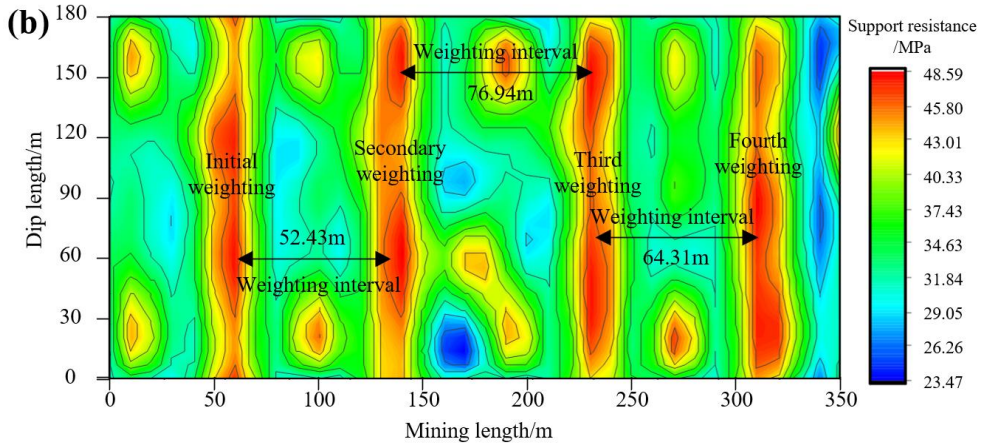

Fig. 13 Contour maps of working face support resistance before and after fracture-induced weakening of CDTHR: (a) before fracture-induced weakening of the CDTHR; (b) after fracture-induced weakening of the CDTHR

5 Conclusions

(1) The ultimate load-bearing strength of CDTHR gradually decreases with an increasing overhanging span and a decreasing maximum normal stress, and it is significantly more sensitive to the overhanging span of the CDTHR. Furthermore, when CDTHR located at a greater distance from the coal seam fracture, the combined load-bearing capacity of the CDTHR in closely spaced competent key strata exhibits a substantially greater reduction. This is because the structural instability and fracturing of high-position CDTHR will trigger a larger-scale caving of the stope roof.

(2) CDTHR play a core role in the strata overlying the coal seam owing to their substantial thickness and robust load-bearing characteristics. Once the CDTHR exceed their load-bearing limits and fracture, the overlying multi-layer strata undergo simultaneous fracturing and caving. Therefore, implementing fracture-induced weakening on CDTHR can effectively disrupt their integrity, reduce their load-bearing capacity, and eliminate long-distance roof-hanging phenomena.

(3) The high-position of the CDTHR serve as the primary storage zones for elastic energy induced by working face mining disturbances. When the low-position CDTHR reach their strength limits and undergo failure, the massive amount of accumulated internal elastic energy is released, which can readily induce intense strata behavior and rock bursts. In addition, rational segmented fracturing and weakening of CDTHR in the stope enables the orderly release of the energy accumulated within them.

(4) Prior to intervention, the stope with CDTHR features large periodic weighting step intervals and ranges, concentrated high stress and energy release, and high working face support resistance. Following the application of staged directional long-borehole hydraulic fracturing technology to weaken the CDTHR in stope, the periodic weighting step intervals and ranges of the working face are significantly reduced, the continuity of high support resistance strips is weakened, the degree of stress and energy concentration release is markedly mitigated, and the threats of working face strata behavior and dynamic disaster are notably ameliorated.

Declaration of competing interest

The authors declare that they have no known competing financial interests or personal relationships that could have appeared to influence the work reported in this paper.

Data availability

The data that support the findings of this study are available from the corresponding author upon reasonable request.

References

He Manchao, Wang Qi, Wu Qunying, (2021). Innovation and future of mining rock mechanics. Journal of Rock Mechanics and Geotechnical Engineering. 13(05), 1-21.

Yu Bin, Gao Rui, Kuang Tiejun, et al, (2025). Engineering study on fracturing high-level hard rock strata by ground hydraulic action. Tunnelling and Underground Space Technology. 86(13), 156-164.

Wu Xuewu, Ma Zhenqian, Zhu Yuankun, et al, (2026). Hydraulic Fracturing Roof Cutting and Pressure Relief for Controlling Mining-Induced Cross-Cut Deformation. International Journal for Numerical and Analytical Methods in Geomechanics. 50(13), 3754-3768.

Zhang Quan, He Manchao, Wang Jiong, et al, (2022). Investigation of a non-explosive directional roof cutting technology for self-formed roadway. International Journal of Mining Science and Technology. 32 (16), 997-1008.

Bai Qiangsheng, Tu Shihao, Wang Fangtian, et al, (2017). Field and numerical investigations of gateroad system failure induced by hard roofs in a longwall top coal caving face. International Journal of Coal Geology. 173(14), 176-199.

Wu Xuewu, Ma Zhenqian, Zhu Yuankun, et al, (2020). Numerical simulation of hydraulic fracture deflection influenced by slotted directional boreholes using XFEM with a modified rock fracture energy model. Journal of Petroleum Science and Engineering. 193(21), 107-121.

Xue Xiaoqiang, Du Wei, Cui Jian, et al, (2025). Roadway roof stability grading method based on multi-index optimization. Scientific Reports. 15(06), 292-303.

Tian Xinyuan, Gong Siyuan, Dou Linming, et al, (2024). Characterize the influences of hydraulic fracturing on preventing rock burst from the stress and vibration fields. Geomechanics and Geophysics for Geo - Energy and Geo - Resources. 10(03), 169-181.

Jing Zehao, Zhou Xihua, Li Yanchang et al, (2024). Research on the technology of uniformly injecting nitrogen into the porous long pipes in the gob of the gob-side entry retaining mining mode with roof cutting and pressure relief. Scientific Reports. 14(08), 205-223.

Li Nan, Wang Enyuan, Ge Maochen, et al, (2014). The fracture mechanism and acoustic emission analysis of hard roof: a physical modeling study. Arabian Journal of Geosciences. 32(12), 213-227.

He Jiang, Dou Linming, Mu Zonglong, et al, (2016). Numerical simulation study on hard-thick roof inducing rock burst in coal mine. Journal of Central South University. 23(03), 2314-2320.

Han Changliang, Zhang Nong, Li Baoyu, et al, (2015). Pressure relief and structure stability mechanism of hard roof for gob-side entry retaining. Journal of Central South University. 22(12), 4445-4455.

Zhao Mengye, Zhu Lei, Huang Qingxiang, et al, (2022). Research on roof fracture characteristics of gob-side entry retaining with roof cutting and non-pillar mining in thick coal seam, China. Geotechnical and Geological Engineering. 40(17), 1429-1448.

Wang Hongwei, Wu Yongping, Liu Maofu, et al, (2020). Roof-breaking mechanism and stress-evolution characteristics in partial backfill mining of steeply inclined seams. Geomatics, Natural Hazards and Risk. 11(01), 2006-2035.

Lin Cong, Deng Jianqiang, Liu Yaoru, et al, (2016). Experiment simulation of hydraulic fracture in colliery hard roof control. Journal of Petroleum Science and Engineering. 128(11), 265-271.

Xu Jizhao, Zhai Cheng, Qin Lei, et al, (2016). Mechanism and application of pulse hydraulic fracturing in improving drainage of coalbed methane. Journal of Natural Gas Science and Engineering. 12(02), 29-42.

Shen Wenlong, Bai Jianbiao, Wang Xiangyu, et al, (2016). Response and control technology for entry loaded by mining abutment stress of a thick hard roof. International Journal of Rock Mechanics and Mining Sciences. 90(19), 26-34.

Lu Caiping, Liu Guangjian, Liu Yang, et al, (2015). Microseismic multi-parameter characteristics of rockburst hazard induced by hard roof fall and high stress concentration. International Journal of Rock Mechanics and Mining Sciences. 76(13), 18-32.

Zhang Quan, Wang Jiong, Guo Shan, et al, (2021). Shaped charge hydraulic blasting: an environmental, safe, and economical method of directional roof cutting. Geofluids. 18(09), 106-127.

Yang Yongkang, Gao Peipeng, Zhang Chao, et al, (2023). Numerical investigation of the influence of roof-cutting parameters on the stability of top coal gob-side entry retaining by roof pre-fracturing in ultra-thick coal seam. Energies. 16(02), 106-120.

Xie Shengrong, Wu Yiyi, Guo Fangfang, et al, (2022). Application of pre-splitting and roof-cutting control technology in coal mining: a review of technology. Energies. 15(07), 106-122.

Bai Libin, Wu Fengfeng, Yang Peiju, et al, (2024). Characteristics of perimeter rock damage in a bottom-pumping roadway under the influence of mining activities and rational location studies: a case study. Applied Sciences. 14(03), 2727-2786.

Wu Hao, Zhu Chuanqu, Li Qingfeng, (2021). Study on surrounding rock stability mechanism of gob-side entry retaining with prefabricated fracture. Advances in Civil Engineering. 21(11), 156-169.

Guo Tiankui, Gong Facheng, Shen Lin, et al, (2019). Multi-fractured stimulation technique of hydraulic fracturing assisted by radial slim holes. Journal of Petroleum Science and Engineering. 174(32), 572-583.

Liu Chenyang, Li Hui, Wu Yiyi, et al, (2025). Initial weighting strength control of thick and hard roof based on pre-splitting blasting of whole roadway roof: numerical model and engineering verification. Results in Engineering, 27(05):106-124.

Shan Pengfei, Yang Ke, Xu Huicong, et al, (2026). Evolution Mechanism and Bearing Capacity of End-Area Hanging Roofs in Thick Hard Roofs with Liquid Nitrogen Fracturing Control. Applied Sciences, 16(09), 419-433.

Dang Jiaxin, Tu Min, Zhang Xiangyang, et al, (2024). Research on the bearing characteristics of brackets in thick hard roof mining sites and the effect of blasting on roof control. Geomechanics and Geophysics for Geo - Energy and Geo - Resources, 10(01), 118-32.

Fu Qiang, Yang Jun, Gao Yubing, et al, (2024). Combined blasting for protection of gob-side roadway with thick and hard roof. Journal of Rock Mechanics and Geotechnical Engineering. 16(08):3165-3180.

Zhang Zhigang, Dai Linchao, Sun Haitao, et al. (2023). Study on the Spatiotemporal Dynamic Evolution Law of a Deep Thick Hard Roof and Coal Seam. Processes, 11(26): 238-249.

Zhang Chen, Zou Junpeng, Zhang Xiufeng, et al. (2022). Study on the Mechanism of Weakening Thick and Hard Roof by Deep-Hole Blasting in Deep Coal Mines. Frontiers in Earth Science, 10(13): 49-62.

Fan Jun, Dou Linming, Hu He, et al, (2012). Directional hydraulic fracturing to control hard-roof rockburst in coal mines. International Journal of Mining Science and Technology. 22(02): 177-181.

Guo Yu, Li Zewei, Isomitdinovich Tukhtaev Bobirjon, er al, (2026). Strata behavior and advanced control technologies in longwall top coal caving of extra-thick coal seams under hard roofs. Scientific Reports. 42(06):126-138.

Zhao Weiwei, Cao Anye, Zhang Ning, et al, (2026). Underground directional hydraulic fracturing of near-field hard roof in coal mines: rockburst prevention mechanism. Geomechanics and Geophysics for Geo - Energy and Geo - Resources. 16(02):122-141.

Zhang Rupei, Gong Siyuan, Cai Wu, et al, (2026). Energy Transfer Mechanism of Hard-Roof Hydraulic Fracturing in Goaf-Side Working Face Based on Microseismic-Driven Damage Model. Sensors. 26(11): 3566-3579.

Yao Zhuangzhuang, Feng Tianxin, Dai Linchao, et al, (2026). T Mechanism and Engineering Practice of Pressure Relief by Hydraulic Fracturing with Directional Long Boreholes in Hard Roof Strata. Applied Sciences ,16(09):4209-42242.

Wu Yiyi, Liu Chenyang, Gao Yubing, et al, (2025). Hydraulic fracturing technology for controlling surrounding rock failure under coal pillar and thick-hard roof conditions: stress-fluid–solid coupling analysis based on multi-scale DEM. Engineering Failure Analysis, 182(53):268-285.

Zou Junpeng, Zhang Quan, Jiang Yujing, et al, (2024). Mechanism of hydraulic fracturing for controlling strong mining-induced earthquakes induced by coal mining. International Journal of Rock Mechanics and Mining Sciences, 181(21): 158-169.

Zhuang Jiaxin, Mu Zonglong, Cai Wu, et al, (2024). Multistage hydraulic fracturing of a horizontal well for hard roof related coal burst control: Insights from numerical modelling to field application. International Journal of Mining Science and Technology, 34(13): 109-125.

Xia Binwei, Zhou Yanmin, Zhang Xingguo, et al, (2024). Physical and numerical investigations of target stratum selection for ground hydraulic fracturing of multiple hard roofs. International Journal of Mining Science and Technology, 34(05): 699-712.